J. Fluid Mech. (2002), *vol.* 461, *pp.* 1–24. © 2002 Cambridge University Press
DOI: 10.1017/S0022112002008479 Printed in the United Kingdom

Whole-field velocity measurements around an axisymmetric body with a Stratford–Smith pressure recovery

By M. HAMMACHE, F. K. BROWAND AND R. F. BLACKWELDER

Department of Aerospace & Mechanical Engineering, University of Southern California, Los Angeles, CA 90089-1191, USA

(Received 9 November 1999 and in revised form 12 November 2001)

Wind tunnel experiments are performed on a body of revolution with aft-section designed to be an axisymmetric Stratford ramp (i.e. the flow over the 'ramp' experiences an adverse pressure gradient that causes it to be continuously on the verge of separation). Digital particle image velocimetry (DPIV) measurements over the ramp reveal a thick boundary layer that is characterized by self-similar velocity profiles with a large wake component and organized vorticity structures. The mean skin friction quickly drops to a value near zero.

The sensitivity of the boundary layer to the degree of severity of the adverse pressure gradient is investigated by testing two additional ramps; one is slightly more conservative (i.e. less steep) than the Stratford ramp while the other is slightly more radical (i.e. steeper). In comparison to the Stratford ramp, the conservative ramp is characterized by a thinner boundary layer, with velocity profiles that start attached and gradually develop a large wake component, a much more gradual drop in the skin friction, and vorticity that is concentrated very close to the wall. On the other hand, the boundary layer over the radical ramp is unsteady and separates intermittently. Measurements of the drag force on each of the three bodies confirm that the Stratford ramp experiences the least amount of drag.

Finally, additional data are gathered on the windward and leeward sides of the Stratford ramp when subjected to a small angle of attack. This case exhibits a more complex flow structure: the flow remains attached over the windward side of the ramp while separating over the leeward side.

1. Introduction

Two important findings resulted from the work of Stratford on turbulent boundary layers in adverse pressure gradients. The first, as reported in Stratford (1959*a*), is an empirical method for predicting the location of separation in a two-dimensional turbulent flow. The general expression is an equation for the shear stress as a function of the pressure coefficient and the rate of change of pressure coefficient along the surface. Separation is predicted to occur at the point of vanishing shear stress. The significant contribution of Stratford is to realize that the empirical expression could be integrated – with the shear stress set equal to zero – to provide a distribution of pressure that would presumably produce a condition of zero shear stress (or incipient separation) *at every point along the surface*. This distribution of pressure, and the

concomitant surface shape, is known as the Stratford criterion of pressure recovery and the shape is referred to as a Stratford ramp.

The Stratford ramp is thus anticipated to be the shortest possible surface over which the maximum recoverable pressure rise occurs without flow separation. (A laminar flow antecedent is due to Prandtl, and is discussed in Schlichting 1979, pp. 220–223). The work of Stratford concerns flows over planar surfaces and constant-radius axisymmetric bodies, and it was not until two decades later that Smith (1977) proposed an extension of the criterion to axisymmetric bodies with changing radius. Hence, the term 'Stratford–Smith criterion' is often used when discussing bodies of revolution that satisfy Stratford's criterion for pressure recovery.

The second finding is documented in Stratford (1959*b*) and concerns the fundamental and practical implications of maintaining a boundary layer on the verge of separation. From a physical perspective, the Stratford ramp is of great interest since it has unique properties related to both boundary layers and mixing layers. Because the flow over the ramp is attached, its characteristics are similar to those of a boundary layer, but it can also be considered to be wake-like because it has near-zero mean shear at the wall. From an engineering point of view, the potential of drag reduction via boundary layer control (in this case through body design) has great appeal.

2. Experimental setup and measurement procedures

2.1. *The design method*

The details of the method used to design the axisymmetric Stratford body are given in Tokumaru, Browand & Blackwelder (1996). The task is considerably more complicated in axisymmetric than planar flow because the appropriate pressure distribution condition contains the (unknown) body shape. Tokumaru *et al.* propose an iterative solution procedure as follows. The body is represented by a series of localized B-splines, B_i, having variable weights, b_i, $i = 1 \rightarrow m$:

$$r(s) = \sum b_i B(s, s_i). \tag{2.1}$$

The pressure coefficient at any point on the body is now regarded as a function of position along the body and the weights, b_i:

$$C_p(s) = C_p(s, b_i). \tag{2.2}$$

An infinitesimal local change in the body shape – equivalent to a change in the value of b from b_i to $b_i + \delta b_i$ – generates a pressure change at any point $s = s_k$, $k = 1 \rightarrow n$, on the body:

$$\delta C_p(s_k) = \sum \frac{\delta C_p(s_k, b_i)}{\delta b_i} \delta b_i + \text{h.o.t.} \tag{2.3}$$

The influence matrix,

$$\frac{\delta C_p(s_k, b_i)}{\delta b_i},$$

is then evaluated by determining δC_p at each of the points s_k for a δb_i change in each of the weights.

The iterative design procedure is begun by first choosing a body shape, thus determining the b_i. The convergence of the method is not particularly sensitive to the initial choice – for example, an ellipsoid of revolution would be satisfactory as in Tokumaru *et al.* The pressure distribution about the body shape, $C_p(s_k, b_i)_{current}$,

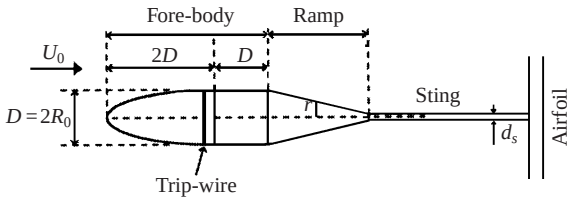

FIGURE 1. Schematic of the body, including support sting (top view).

is computed by standard methods (by utilizing a panel code plus a boundary layer correction, or a Reynolds-averaged Navier–Stokes calculation). The influence matrix,

$$\frac{\delta C_p(s_k, b_i)}{\delta b_i},$$

is computed next and $C_p(s_k, b_i)$ is made closer to the desired distribution by forming

$$\delta C_p(s_k) = C_p(s_k, b_i)_{desired} - C_p(s_k, b_i)_{current} \tag{2.4}$$

and determining the required new body shape – the δb_i – by inverting the linear expression (2.3). The pressure distribution about the new body is computed and the previous steps are repeated. In practice, the procedure converges in five to ten iterations, and it is only necessary to compute the influence matrix several times. Two options are available: The first is to prescribe a given pressure distribution for the entire body, then use the method to determine the shape. The second option is to specify a preset geometry for the forward portion of the body and to predict the shape of the back section that will produce a maximum pressure rise without flow separation. This latter option is selected; Tokumaru (1996) may be consulted for further details.

2.2. *The bodies*

A sketch of the body geometry used in this study is shown in figure 1. The fore-body consists of a hollow half-ellipsoid of base diameter $D = 2R_0 = 15.2\,\text{cm}$ and aspect ratio 4 : 1, followed by a section of constant radius R_0 and of length $L = 2R_0$. The aft-section, which resembles a cone – although the radius of curvature does not vary linearly along the axis – is the actual Stratford ramp. The near-conical shape is a result of the imposed fore-body shape, as explained in the previous section.

The ramp is made of a plastic material that is cast in a mould and then machined to the desired shape with a CNC milling machine. The ramp is fitted to the fore-body by an interlocking slot that provides accurate alignment, so that there is no discontinuity in the surface of the body at the junction. The downstream end of the ramp ends in a support sting that consists of a steel pipe of constant diameter $d_s = 1.90\,\text{cm}$. The downstream end of the sting is secured to an airfoil whose axis is perpendicular to the flow direction.

During the casting phase, a number of static pressure ports are placed along the ramp and connected to thin nylon tubes that are passed outside of the body through the support pipe. An additional four pressure ports whose function is to assist in aligning the body with the free-stream direction are provided around the nose of the fore-body. These ports are located 2.54 cm downstream of the nose tip and are positioned on a circle normal to the axis of symmetry, equally spaced at 90° intervals. Gradually pitching or yawing the body until the pressures recorded by these four static ports are equalized guarantees zero angle of attack.

Ramp	Conservative, $\alpha = 0$	Stratford, $\alpha = 3°$ Windward side	Stratford, $\alpha = 0$	Stratford, $\alpha = 3°$ Leeward side	Radical, $\alpha = 0$
Angle to free stream	22°	23°	26°	29°	29°
AGP	⟶	Increasingly	aggressive	ramps	⟶

TABLE 1. The different test conditions and the corresponding angles between ramp and free-stream.

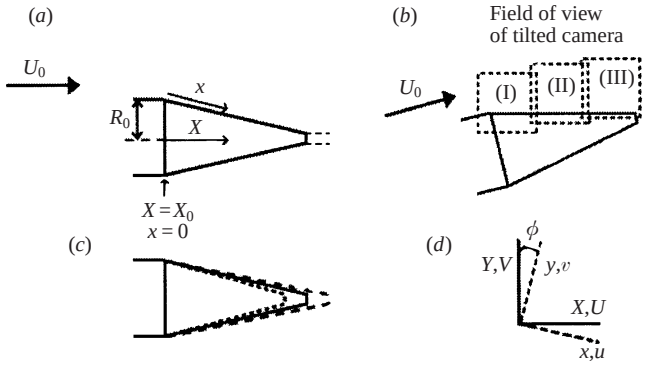

FIGURE 2. Schematics of the ramps and coordinate systems. (*a*) Ramp in different frames of reference. (*b*) Three dashed squares indicate fields of view of PIV camera. (*c*) Schematic of the three ramps: ——, Stratford ramp; – – –, conservative ramp; · · · ·, radical ramp. (*d*) Coordinate systems.

The body is specifically designed to achieve incipient separation over the ramp at a Reynolds number $R_e = U_0 D/\nu$ of 2×10^5. The design code prescribes a specific mean turbulent boundary layer velocity profile at the beginning of the ramp at this Reynolds number and iterative measurements established that such a profile is obtained by placing a trip wire around the fore-body at a distance $L = 2.34R_0$ upstream of the start of the ramp. The body is supported in the wind tunnel by a sting starting at the downstream end of the ramp. In the axisymmetric Stratford flow, it is suspected that the presence of the sting may affect the flow, but only at the rearmost portion of the ramp.

A perturbation study of the Stratford ramp is conducted by testing other ramp configurations (which are combined with the same fore-body), namely:

(i) two new ramps, which are referred to as the 'conservative' and 'radical' ramps, and which are obtained by stretching and compressing, respectively, the Stratford ramp by 15% along its axis;

(ii) the Stratford ramp body subjected to a small angle of attack $\alpha = 3°$ – this case produces two distinct data sets: the flow over the windward and leeward sides of the ramp.

Table 1 summarizes the five test conditions and lists the angles of the different ramps with respect to the free stream. The ramp angle (ϕ) could be used as a parameter to classify the severity of the adverse pressure gradient (APG) along the various ramps, with increasingly larger angles signifying more aggressive ramps and thus a more severe APG. All the ramps have the same base and tip diameters and are fitted to the same fore-body, as shown in figure 2. The boundary layer along the fore-body is tripped at the same location as specified above and the free-stream velocity is kept constant at $U_0 = 20\,\mathrm{m\,s^{-1}}$.

2.3. *The flow facility and measurement techniques*

The experiments are conducted in USC's Dryden wind tunnel, which is a recirculating flow facility with a free-stream maximum speed of approximately $30\,\mathrm{m\,s^{-1}}$. The test section is 6.1 m long and has an octagonal cross-section with sides measuring 57 cm. The contraction ratio between the test section and the settling chamber is approximately 1/10. The free-stream velocity U_0 is kept constant at $20\,\mathrm{m\,s^{-1}}$ in all experiments. At this speed, the turbulence level is approximately 0.1% of the free stream (see LeBlanc, Blackwelder & Liebeck 1990).

The streamwise distribution of wall static pressure along the test section is measured with static ports that are equally spaced along the top wall, at intervals of 15.24 cm. The surface static pressure ports on the fore-body and ramp are connected to a Scanivalve wafer switch and sampled by a MKS Baratron pressure transducer.

Preliminary measurements of the ramp pressure distribution show pressure recovery and mean-velocity profiles taken with a hot-wire anemometer indicate that the mean skin-friction velocity is close to zero, providing a first confirmation that the design method described in § 2.1 does indeed predict the correct shape for an axisymmetric Stratford ramp. However, since the objective is to gain a detailed global view of the flow along the ramp, it is clear that hot-wire anemometry is not well suited for this purpose because hot-wire anemometers only produce single-point measurements and are less reliable in separated or nearly separated flows. A better measurement technique is needed, and digital particle image velocimetry (DPIV) is selected for its capability of measuring two components of velocity over an entire field at once. The reader is referred to Fincham & Spedding (1997) for the details of the technique. Clearly, DPIV measurements cannot resolve the region near the wall very accurately, but this is not a concern since the boundary layer in a strong APG is known to be thick. The main goal is to obtain a global view of the flow, with detailed velocity profiles everywhere in the boundary layer except very close to the wall. Measurements obtained with this system have demonstrated its usefulness in quickly gathering both instantaneous and statistical whole-field data.

All DPIV measurements are obtained in the vertical plane of symmetry of the body. The technique used here is two-dimensional, so that no out-of plane (azimuthal) displacements are measured. The flow is seeded with a fog of micron-size droplets formed far upstream of the body and allowed to circulate in the tunnel a few times to produce a uniform distribution of particles that track the flow closely. The flow field is illuminated with light sheets formed with the co-linear beams generated by two pulsed ND-Yag lasers operating at a repetition rate of 10 Hz. Each light pulse has a duration of 5 ns and an energy output of 160 mJ. The particle images are recorded by a digital camera equipped with a square CCD with a resolution of approximately one million pixels, and are transferred digitally onto a desktop PC where they are processed to yield instantaneous two-dimensional data fields.

During image acquisition, the ramp can be imaged through lenses of various focal lengths that produce different degrees of magnification of the flow field. Clearly, a higher magnification produces better spatial resolution, but with the drawback that the measured area is smaller. This translates into an increasingly large number of independent data sets as magnification is increased. Consequently, a compromise has to be reached that satisfies the requirements of sufficient spatial resolution and manageable amount of data. The flow over the entire ramp could only be obtained by imaging several contiguous fields that are later combined in a montage.

In the present case the camera is tilted so that the bottom edge of the CCD is aligned with the ramp and the flow field is divided into three areas, with a region of overlap between them, as shown in figure 2(*b*). The frame of reference used in the DPIV data is such that the x and y coordinates, and the corresponding velocity components (u and v), are tangential and normal to the wall of the ramp respectively.

The images cover a flow area of approximately 80 mm × 80 mm and are processed using square interrogation windows of approximately 3.24 mm^2, producing vector fields of approximately 90 × 90 vectors, with a spatial resolution of approximately 0.9 mm. Such resolution is adequate over most of the flow field since the boundary layer thickness grows to several centimetres. However, the boundary layer is much too thin and the velocity gradients too high near the beginning of the ramp to be completely resolved with DPIV.

A series of approximately 100 image pairs is obtained over each area and processed to obtain quasi-instantaneous and statistical quantities, such as the average in-plane velocity components ($\bar{u}$, $\bar{v}$) and the root-mean-square of their fluctuations ($\overline{u'^2}$, $\overline{v'^2}$), as well as the growth rates of the physical, displacement and momentum thicknesses (δ, δ_1 and δ_2) of the boundary layer over the ramp.

3. Results

3.1. *The Stratford ramp at* $\alpha = 0$

Pressures are measured at 25 stations along the pressure recovery (and at 18 stations upstream of the recovery). The presence of a sharp pressure dip just before the region of pressure recovery introduces some difficulty in predicting the velocity profile in that region, and produces a body that is slightly on the conservative side. However, there is excellent agreement between the expected design pressure distribution and the measured pressure all the way through the pressure recovery region, as shown in figure 3(*a*). (Figure 3*b* plots the local radius of curvature of the ramp, r/R_0, and its first and second derivatives with respect to the axial coordinate X.) The total length of the pressure recovery ramp is $2.2 \times R_0$, and the accumulated static pressure recovered is approximately 43% of $q_{freestream}$.

In order to achieve good spatial resolution from the DPIV data, the flow field is divided into three separate regions as indicated in figure 2(*b*): region (I) starts just upstream of the beginning of the ramp, region (II) covers the middle of the ramp and region (III) extends to the downstream tip of the ramp, with sufficiently large regions of overlap between contiguous regions so that the data sets can be patched together. The data in each region are processed to yield measurements of the averaged velocity components and their root-mean-squares and of the average out-of-plane vorticity component, which is obtained by direct differentiation of the two-dimensional velocity field. Note that the images are taken with the bottom edge of the CCD aligned with the slope of the ramp as outlined in § 2.3, so that $\bar{u}$ and $\bar{v}$ are tangential and normal, respectively, to the ramp.

The time-averaged velocity vector field indicates that the flow gradually aligns itself with the ramp once it has turned the shoulder at the end of the fore-body and start of the pressure recovery ramp (region I in figure 2*b*). The plots are not shown because of the small scale of the vectors near the wall, especially at the most downstream end of the ramp (region III). Instead, it is preferable to use intensity plots, which are maps of the magnitude of the quantity of interest.

The magnitudes of $\bar{u}$ and $\bar{v}$ and of the out-of-plane vorticity component $\bar{\omega}$ are plotted on figure 4. The maximum and minimum value of each quantity is represented

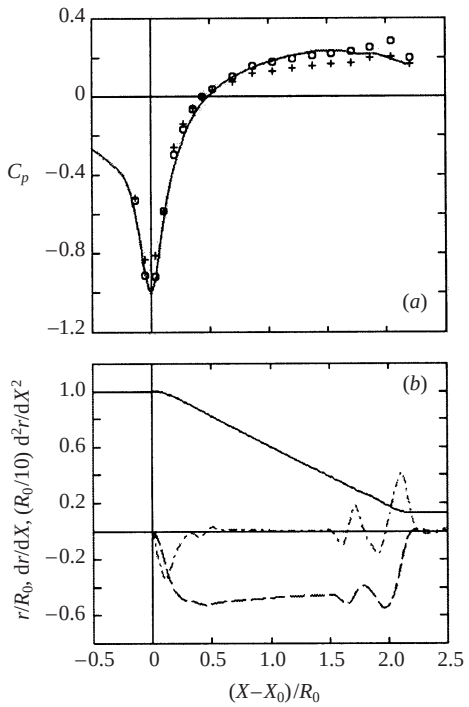

FIGURE 3. Pressure recovery measurements and theory for the Stratford ramp at $\alpha = 0$. (*a*) Distribution of C_p over the ramp: ——, panel method with boundary layer; +, measurements with trip located at $X - X_0 = -2.34R_0$; ○, measurements with trip at $X - X_0 = -0.25R_0$. (*b*) r/R_0 (——), dr/dX (– – –) and $10^{-1}R_0\, d^2r/dX^2$ (— · —).

by black and white, respectively. Note that the data over the ramp are made up of three distinct sets that are patched together. A black line represents the ramp itself. The plots of $\bar{u}$ and $\bar{v}$ show a region of acceleration of the flow at the beginning of the ramp, followed by a gradual deceleration as the flow realigns itself with the wall-tangential direction. Note the good agreement of the three quantities in the regions of overlap.

The mean vorticity appears to be mainly concentrated near the wall at the start of the ramp, where the boundary layer is thin and where a region of strong acceleration is located. Clearly, the flow negotiates the turn and remains attached. Downstream from the turn, the mean vorticity rapidly diminishes throughout the boundary layer. However, two regions of elevated vorticity persist over the first half of the ramp: one near the wall, a second in the second half of the boundary layer. Along the second half of the ramp, the outer vorticity peak continues to diminish. The inner peak continues to move away from the wall, to a position about one-half of the boundary layer thickness. Mean vorticity plots such as this one – and the instantaneous vorticity field images to be discussed – provide the clearest indication of the flow field structure that distinguishes the various ramps.

It is first desirable to determine how the trip wire size and position on the fore-body changes the overall picture of the flow over the ramp. To answer this question, a series of measurements are performed with the following boundary layer trip conditions:

(*a*) trip wire of height 0.8 mm placed at $2.34R_0$ upstream of the start of the ramp;
(*b*) trip wire of height 1.5 mm placed at $2.34R_0$ upstream of the start of the ramp;
(*c*) trip wire of height 1.5 mm placed at $3R_0$ upstream of the start of the ramp.

FIGURE 4

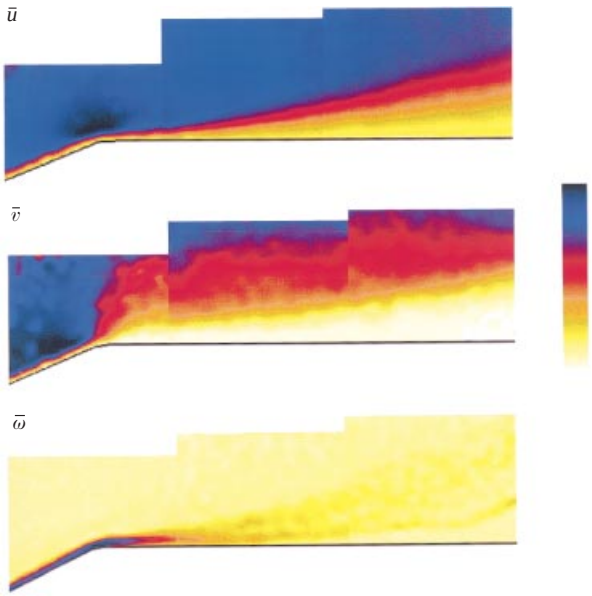

FIGURE 5

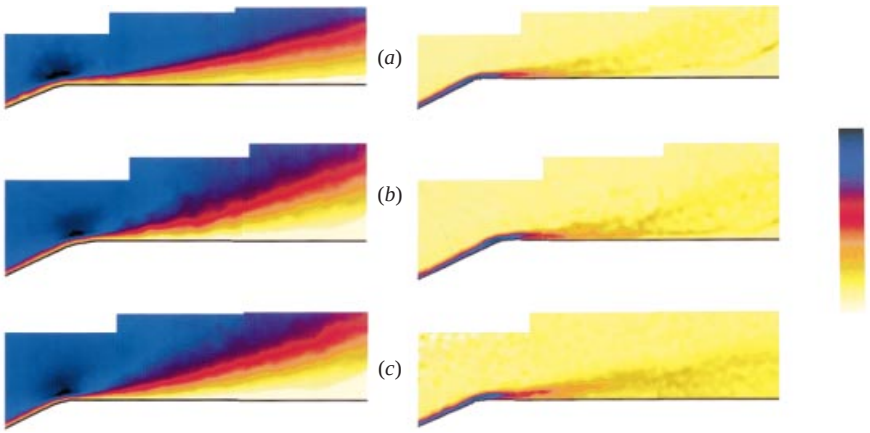

FIGURE 9

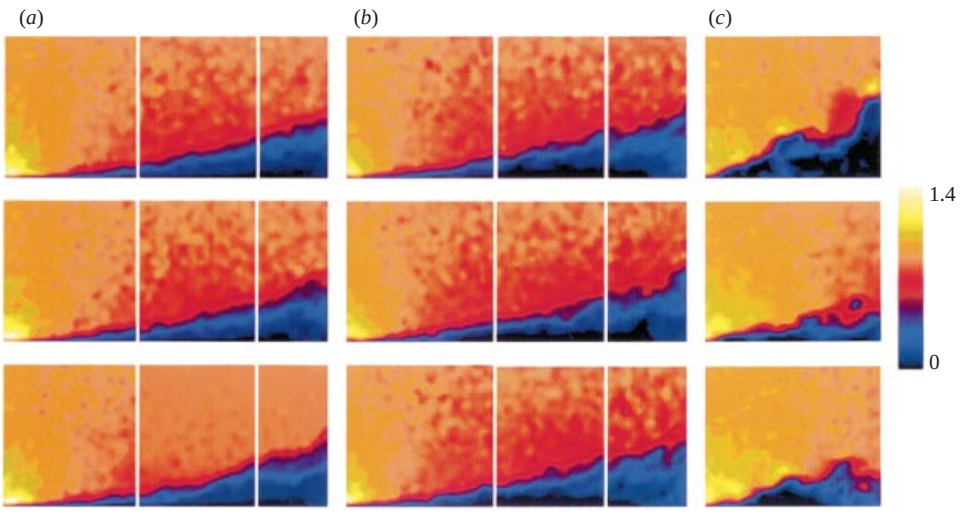

Plots of $\bar{u}$ and $\bar{\omega}$ averaged over 100 instantaneous realizations are shown in figure 5. These clearly indicate that the boundary layer becomes thicker as the trip wire is made thicker or moved upstream. Qualitatively, the boundary layer does not change significantly and does not separate even in the last case where the tripping condition is the most extreme. The body geometry thus appears to be robust enough to these trip conditions, which would indicate that the design could probably be made somewhat more radical, i.e. with a steeper ramp profile. All measurements described hereafter are taken with the thin trip wire (0.8 mm) placed $2.34R_0$ upstream of the beginning of the ramp.

The pressure coefficient decreases gradually over the surface of the cylinder as the ramp is approached, as reflected in figure 3(*a*). At a position 3.3 cm ($0.435R_0$) upstream of the origin, the C_p value is -0.225, corresponding to a local increase in velocity above free stream, $U_{local}/U_0 \approx 1.107$. For reference purposes, boundary layer measurements were made with a hot wire just downstream from the pressure port, and just upstream from the origin of the ramp. The thinness of the boundary layer in this region makes accurate measurements difficult, but at a position 2.5 cm ($0.34R_0$) ahead of the ramp, the boundary layer momentum thickness is approximately 0.74 mm, and the displacement thickness is 1.1 mm.

Mean velocity profiles, extracted from the DPIV data at several streamwise stations along the ramp, are plotted on figure 6. The profiles along the upstream and downstream halves are plotted on two separate figures for more clarity. Boundary layer thickness, δ, is determined to be the point where the vorticity reaches 3% of the maximum value. U_{edge} is the velocity magnitude at the edge of the boundary layer. The profiles quickly develop a large wake component, which is characteristic of nearly separated boundary layers, and appear to achieve self-similarity as the flow progresses along the ramp.

3.2. *The conservative and radical ramps*

A comparison of the mean velocity profiles among the various ramps at $\alpha = 0$ is useful. Figure 7 shows the evolution of the velocity profiles along the conservative ramp. The data indicate that the flow over the upstream part of the ramp is attached, and the velocity profiles gradually achieve a Stratford-like shape over the downstream half. In comparison, the profiles over the Stratford ramp appear to achieve self-similarity much earlier.

On the other hand, the DPIV data obtained over the radical ramp suggest that the flow is separated and reveal the presence of considerable out-of-plane (azimuthal) flow components, at least intermittently. This point is illustrated by figure 8, which shows two instantaneous velocity vector fields recorded a few seconds apart from each other. The dramatic differences between these two vector plots are indicative of the wide variation in the nature of the boundary layer over time. While the flow in figure 8(*a*) appears to be attached for the most part, figure 8(*b*) shows large vortex structures even as far away from the wall as $y/R_0 \simeq 1.25$. The adverse pressure gradient over the radical ramp is too great for the flow to remain attached. Furthermore, the point of separation probably moves along the ramp and separation is not likely to occur

FIGURE 4. Time-averaged intensity plots of $\bar{u}$, $\bar{v}$ and $\bar{\omega}$ over the Stratford ramp at $\alpha = 0$.
FIGURE 5. Intensity plots of $\bar{u}$ (left) and $\bar{\omega}$ (right) over the Stratford ramp at $\alpha = 0$ for various tripping conditions. Refer to text for explanation of tripping conditions (*a*), (*b*) and (*c*).
FIGURE 9. Three sample instantaneous maps of the in-plane velocity magnitude over (*a*) the conservative ramp, (*b*) the Stratford ramp and (*c*) the radical ramp.

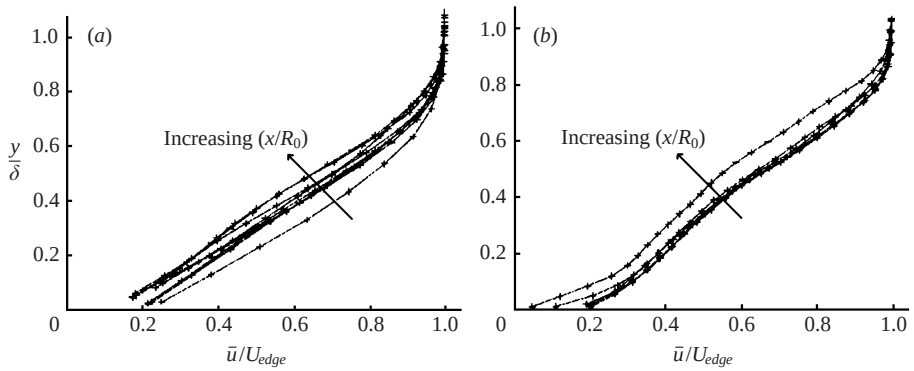

FIGURE 6. Evolution of the mean velocity profile along the Stratford ramp at $\alpha = 0$: (*a*) $x/R_0 = 0.87$–1.39, in increments of 0.087; (*b*) $x/R_0 = 1.57$–2.27, in increments of 0.175.

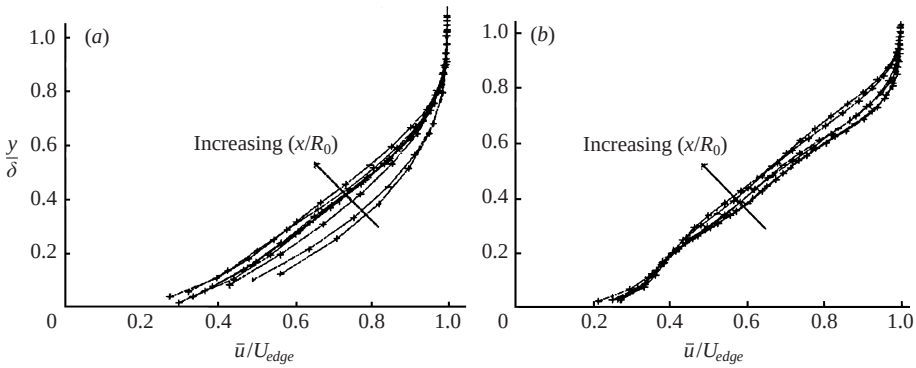

FIGURE 7. Evolution of the mean velocity profile along the conservative ramp: (*a*) $x/R_0 = 0.87$–1.39, in increments of 0.087; (*b*) $x/R_0 = 1.57$–2.27, in increments of 0.175.

uniformly at all azimuthal locations. This is evidenced by the fact that the velocity vectors in some instantaneous realizations indicate the presence of flow out of the plane of symmetry of the ramp.

A set of three instantaneous plots of the velocity magnitude for each of the ramps are shown on figure 9. The intensity maps are normalized with the incident free-stream velocity. Again, the data over the Stratford and conservative ramps is made up of three distinct data sets. The thin lines in the figure indicate where the data sets are patched together. The radical ramp is short enough to be almost entirely covered by a single data set. Most of the radical ramp is shown here in a single patch. The maximum velocity magnitude is measured at the start of the ramps, where the flow accelerates to a velocity above the free-stream value. As the ramp is made more radical, the boundary layer becomes thicker and the flow increasingly unsteady. The boundary layer is thinner and steadier over the conservative ramp than over the Stratford ramp. As the ramp angle is made more radical the boundary layer experiences unsteady separation.

To gain more insight into the differences among the boundary layers over the three ramps at $\alpha = 0$, the average quantities $\bar{u}/U_0$, $\bar{v}/U_0$, $\sqrt{\overline{u'^2}}/U_0$ and $\bar{\omega}R_0/U_0$ are plotted on figures 10(*a*) to 10(*d*), respectively. The plot of $\bar{u}$ shows that the boundary layer over the Stratford ramp starts to grow rapidly, right from the beginning of the ramp. In contrast, the boundary layer over the conservative ramp grows a little

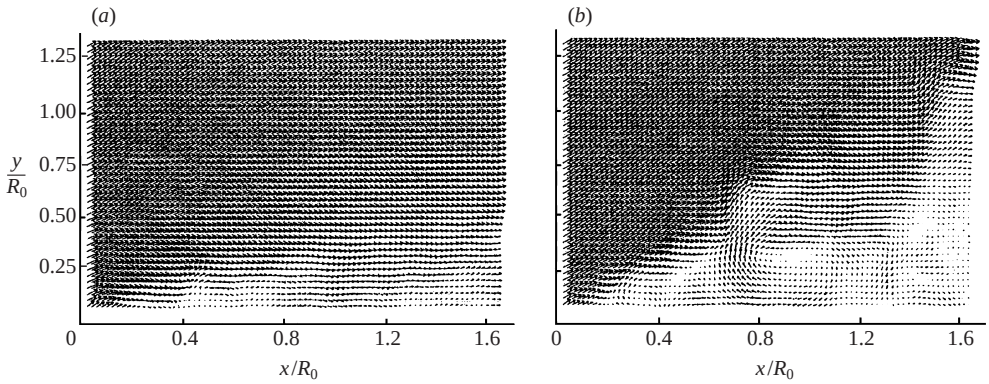

FIGURE 8. Sample instantaneous vector plots of the in-plane velocity components over the radical ramp taken a few seconds apart.

more gradually, and the radical ramp exhibits what looks like a separation bubble. The v-component plots indicate that while the Stratford and conservative ramps do a good job of realigning the outer flow from the free-stream direction to a direction parallel to the ramp, the radical ramp is too steep and causes the flow to separate. Thus the wake behind the conservative and Stratford ramps is likely to be narrower than the wake behind the radical ramp. The vorticity field is concentrated along the wall for the conservative ramp, somewhat in the middle of the boundary layer for the Stratford ramp and furthest from the wall for the radical ramp.

The boundary layer thickness, displacement thickness and momentum thickness for the three ramps at $\alpha = 0$ are plotted on figures 11(a), 11(b) and 11(c). While the definition of δ is the customary normal distance from the wall to the point where the local velocity reaches a specified fraction of the free-stream value, the quantities δ_1 and δ_2 can be defined in different ways. Patel, Nakayama & Damian (1974) suggest the following:

the 'physical definitions', δ_1^*, δ_2^*;

the 'basic planar definitions', $\bar{\delta}_1$, $\bar{\delta}_2$;

the 'usual axisymmetric definitions', δ_1, δ_2.

The 'physical definitions' are given by

$$\int_{R_0}^{R_0+\delta_1^*\cos\phi} 2\pi r\rho U_p \,\mathrm{d}r = \int_{R_0}^{R_0+\delta\cos\phi} 2\pi r\rho(U_p - U)\,\mathrm{d}r \tag{3.1}$$

and

$$\int_{R_0}^{R_0+\delta_2^*\cos\phi} 2\pi r\rho U_p^2 \,\mathrm{d}r = \int_{R_0}^{R_0+\delta\cos\phi} 2\pi r\rho U(U_p - U)\,\mathrm{d}r, \tag{3.2}$$

where $r = R_0 + y\cos\phi$, and U_p is the velocity distribution which would occur if the flow were potential right up to the wall.

Patel *et al.* state that the 'basic planar definitions'

$$\bar{\delta}_1 = \int_0^{\delta} \left(1 - \frac{U}{U_\delta}\right) \mathrm{d}y, \tag{3.3}$$

$$\bar{\delta}_2 = \int_0^{\delta} \frac{U}{U_\delta}\left(1 - \frac{U}{U_\delta}\right) \mathrm{d}y, \tag{3.4}$$

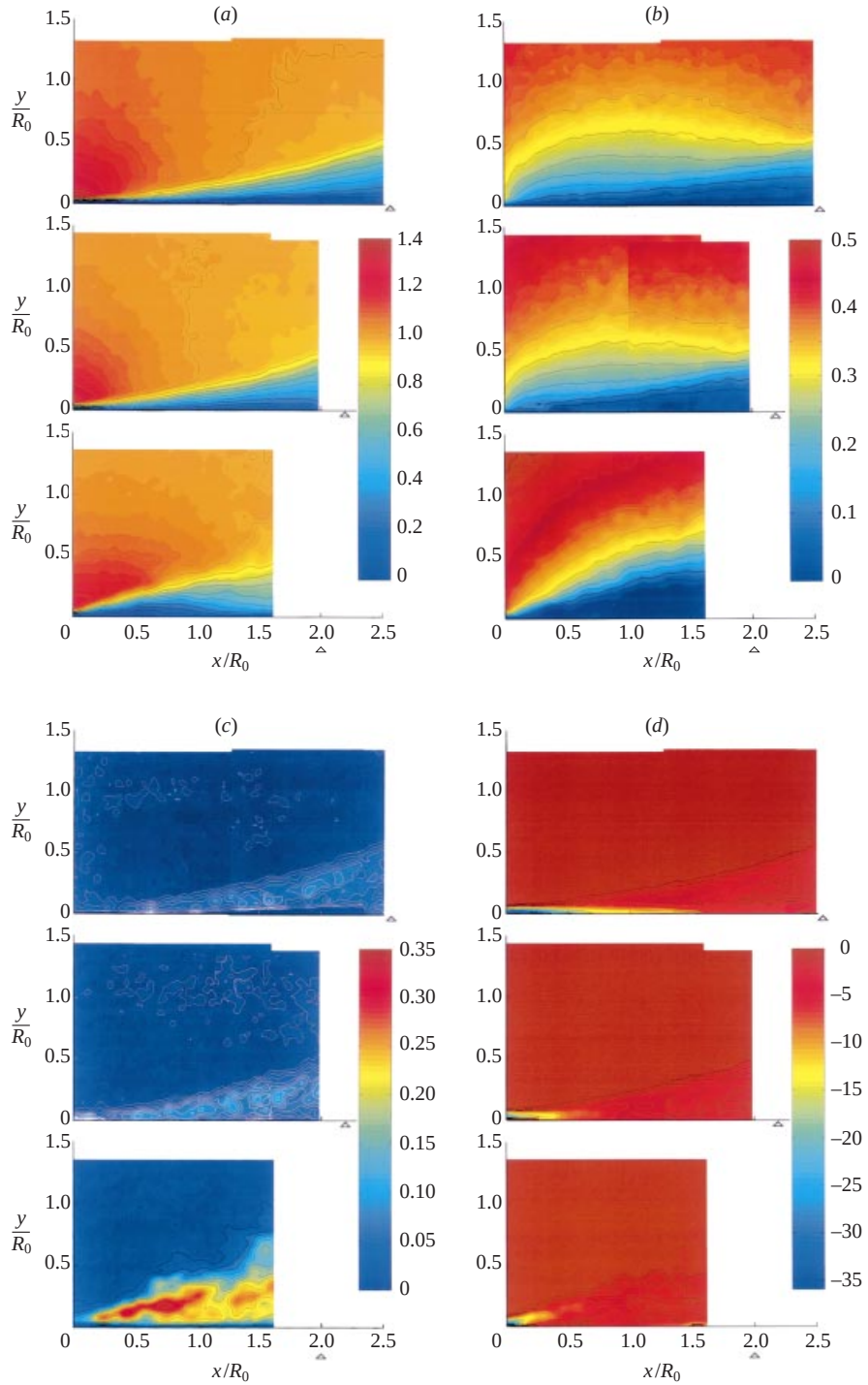

FIGURE 10. Intensity plot of (*a*) $\bar{u}/U_0$, (*b*) $\bar{v}/U_0$, (*c*) $\sqrt{\overline{u'^2}}/U_0$, (*d*) $\bar{\omega}R_0/U_0$ over the conservative, Stratford and radical ramps (from top to bottom) at $\alpha = 0$. $\triangle$ symbol indicates end of ramp.

are useful in 'describing the shape of the velocity profiles, without regard to the geometry of the surface...' and that the 'usual axisymmetric definitions',

$$\delta_1 = \int_0^{\delta} \left(1 - \frac{U}{U_\delta}\right) \frac{r}{R_0}\, \mathrm{d}y, \tag{3.5}$$

$$\delta_2 = \int_0^{\delta} \frac{U}{U_\delta} \left(1 - \frac{U}{U_\delta}\right) \frac{r}{R_0}\, \mathrm{d}y, \tag{3.6}$$

'enable the momentum-integral equation... to be written in a form that is simple and very similar to that for plane-surface boundary layers... [but] lead to some anomalies when the boundary layer is thick in comparison with the local radius of curvature...'

Finally, 'the usual axisymmetric definitions are related to the physical definitions (using $U_p \approx U_\delta$)' by

$$\delta_1 = \delta_1^* \left(1 + \frac{1}{2}\left(\frac{\delta_1^*}{R_0}\right) \cos\phi\right), \tag{3.7}$$

$$\delta_2 = \delta_2^* \left(1 + \frac{1}{2}\left(\frac{\delta_2^*}{R_0}\right) \cos\phi\right). \tag{3.8}$$

In the present work, the displacement thickness and momentum thickness are calculated according to the 'physical' definitions, which appear to be best suited to the current situation. The boundary layer thickness, δ, is computed as the distance from the wall to the point where the vorticity has decreased to 3% of its maximum value. For the sake of simplifying notation, the asterisk is omitted and these quantities are now denoted δ, δ_1 and δ_2 respectively in figures 11(a), 11(b) and 11(c). The regions of data overlap are evident in the figures for the Stratford and conservative ramps.

A measure of the effectiveness of the Stratford ramp in reducing the mean skin friction coefficient is provided by figure 12. The Stratford and conservative ramps are both characterized by a mean skin friction that decreases with downstream distance. However, while the skin friction reaches its minimum value faster over the Stratford ramp, it decreases much more gradually over the conservative ramp. The supposed separation and subsequent reattachment of the flow over the radical ramp produces a steep drop followed by a rise of the skin friction, outlining the extent of the separation bubble at $x/R_0 \leqslant 1.3$. It is worth noting that the mean skin friction remains positive, even for the radical ramp. This could be explained by the notion that separation is intermittent and the flow travels upstream only a small fraction of the time. Another explanation could be that the skin friction over the radical ramp cannot be measured accurately due to the intermittent azimuthal flow components. Nevertheless, the plot in figure 12 offers useful information about the relative distribution of the skin friction for the other two ramps.

3.3. *The Stratford ramp at* $\alpha = 3^\circ$

In this set of experiments, the Stratford ramp (supported by the sting) is pitched by a small angle of attack $\alpha = 3^\circ$. A set of three instantaneous plots of the velocity magnitudes over the windward and leeward sides of the ramp is shown on figure 13, again normalized by U_0. The windward and leeward sides appear to behave like the conservative and radical ramps respectively. The measurements indicate that the boundary layer becomes thicker and less steady as the angle on the leeward side increases.

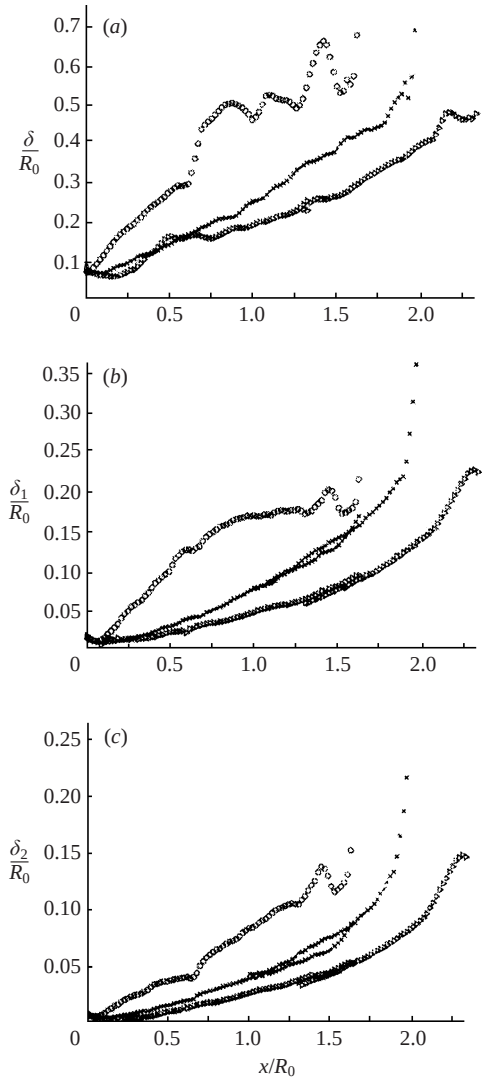

FIGURE 11. Growth of (*a*) boundary layer thickness, (*b*) displacement thickness and (*c*) momentum thickness, according to the 'physical definition': ×, Stratford ramp; ▷, conservative ramp; ○, radical ramp.

Average quantities are shown in figure 14, which contains intensity plots of $\bar{u}/U_0$, $\bar{v}/U_0$, $\sqrt{\overline{u'^2}}/U_0$, and $\bar{\omega}R_0/U_0$ for the Stratford ramp at $\alpha = 0$ and the leeward side of the case at $\alpha = 3^\circ$. The boundary layer is measurably thicker and the level of velocity fluctuation is much higher in the pitched case, indications of intermittent separation. The fact that the flow is prone to separation at such a small angle of attack is further indication that the current body design is quite close to a true Stratford ramp.

Profiles of various quantities can be extracted along lines normal to the Stratford ramp at $\alpha = 0$ and $\alpha = 3^\circ$ (leeward side), at regular intervals along the ramp. Six profiles for the quantities $\bar{u}/U_0$, $\sqrt{\overline{u'^2}}/U_0$ and $\bar{\omega}R_0/U_0$ are shown in figures 15(*a*), 15(*b*) and 15(*c*) respectively. These quantities are plotted against the wall-normal coordinate normalized by the local displacement thickness. Clearly, the flow remains attached

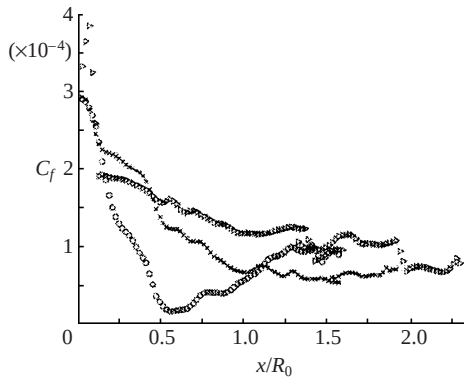

FIGURE 12. Streamwise distribution of the mean skin friction over all ramps: ×, Stratford ramp; ▷, conservative ramp; ○, radical ramp.

in the case $\alpha = 0$, but with wall friction velocity decreasing with the downstream distance. Initially the vorticity has a (negative) maximum value at the wall. The wall maximum rapidly diminishes with increasing downstream distance, and a second local maximum appears away from the wall at a distance of order $y \approx \delta_1$. The peak in $\sqrt{\overline{u'^2}}/U_0$ is situated near to this secondary vorticity maximum, and lies the range 0.08–0.10. Fluctuation levels for values of x/R_0 of 0.22–1.0 collapse on a single plot when scaled with U_0.

In contrast, the case of $\alpha = 3^\circ$ exhibits a flow reversal near the wall for $x \geqslant 2.0$ cm. A much more significant peak of (negative) vorticity develops in the middle of the layer. Fluctuation levels of the u-component of velocity here are in the neighbourhood of 25–35%, as would be characteristic of a separated shear layer. Further downstream, the shear-layer-region vorticity diminishes, probably as a result of azimuthal flow from the windward side of the body. Fluctuation levels do not collapse when scaled with the reference tunnel velocity, U_0.

Evidence of major differences between the two cases is also provided by figure 16, where a series of eight instantaneous vorticity fields over the two ramps is plotted. The vorticity is mostly confined to the wall region in the case $\alpha = 0$, which is characteristic of an attached boundary layer. The middle of the boundary layer is dominated by small patches of negative (clockwise) vorticity (indicated in a darker colour). These structures are conjectured to be similar in their nature to the spanwise rollers observed by Spalart & Leonard (1987) in a DNS simulation of equilibrium turbulent boundary layers, and by Zhang & Fasel (1997) in a more recent numerical simulation of a two-dimensional Stratford ramp. In contrast, the body at $\alpha = 3^\circ$ is characterized by a clear departure of the flow away from the wall. The vorticity patches move significantly further away from the wall in an intermittent fashion. With this outward movement, regions of concentrated negative vorticity (indicated in a lighter colour) appear very close to the wall. This demonstrates that a small angle of attack separates the flow, and produces a vorticity distribution that is more typical of a mixing layer than of a boundary layer.

Further evidence of this distinction between the two ramps is found in figure 17 which plots the growth of δ, δ_1 and δ_2 over the ramps. There is a clear indication of significantly faster growth rates of all three layers in the case $\alpha = 3^\circ$. Finally, figure 18 compares the shape factors (given by $H = \delta_1/\delta_2$) for the two ramps. In the range of $x/R_0 = 0.2$–1 the Stratford ramp at $\alpha = 0$ has a shape factor in the range 2.41–2.84,

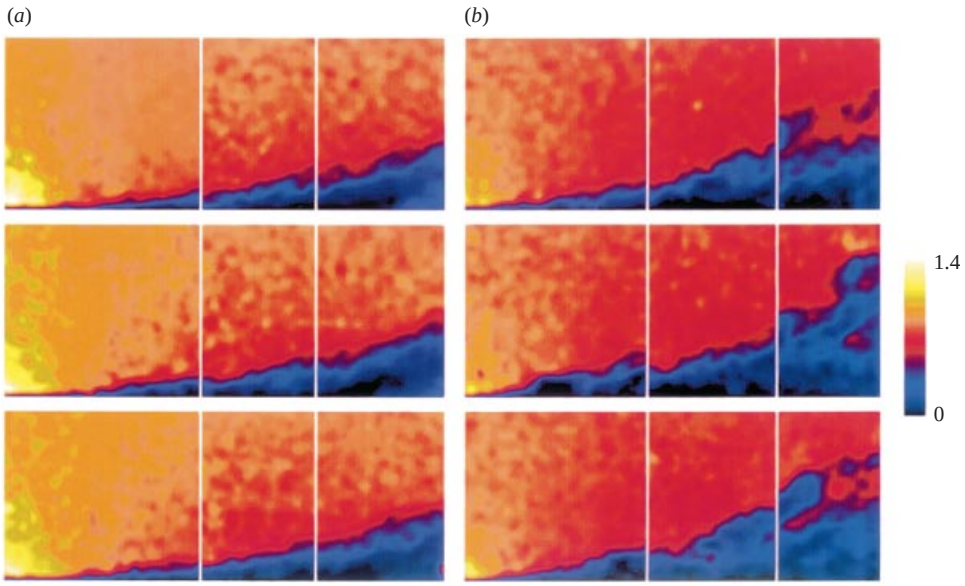

FIGURE 13. Three sample instantaneous maps of the in-plane velocity magnitude, normalized by U_0, over (a) the windward and (b) leeward sides of the Stratford ramp at $\alpha = 3°$.

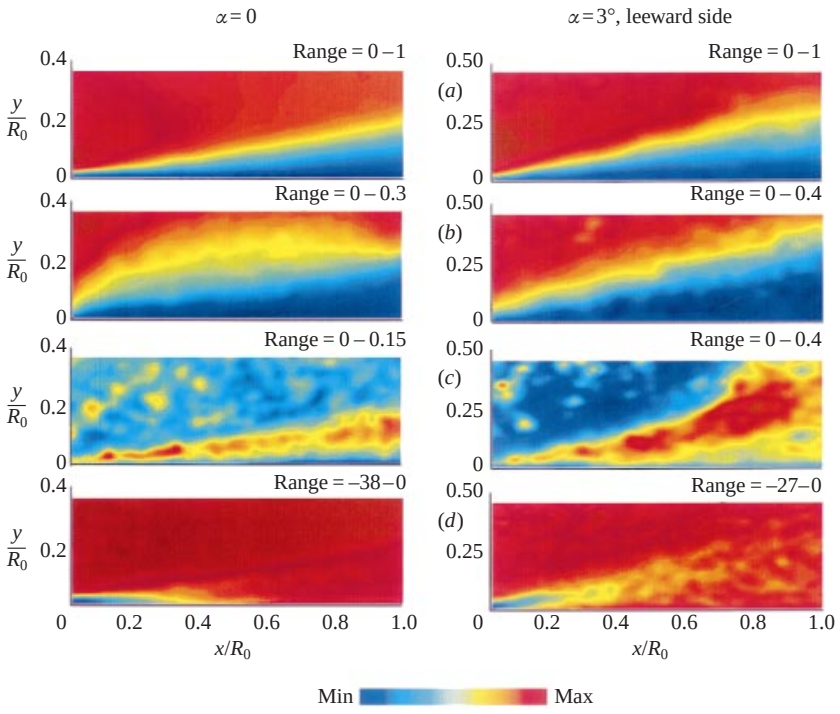

FIGURE 14. Comparison of statistical quantities of flow over the Stratford ramp at $\alpha = 0$ and 3°. (a) $\bar{u}/U_0$, (b) $\bar{v}/U_0$, (c) $(\overline{u'^2})^{1/2}/U_0$, ($d$) $\bar{\omega}R_0/U_0$.

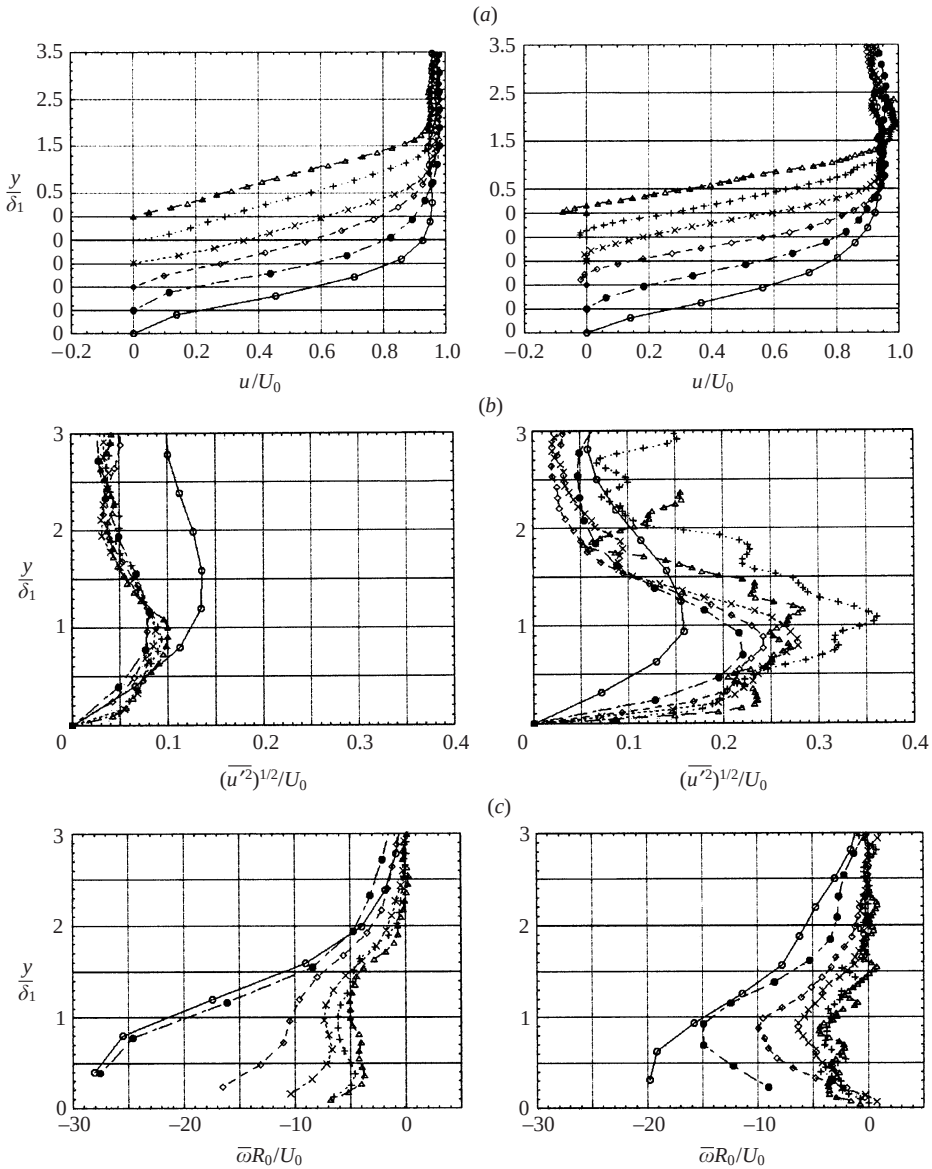

FIGURE 15. Profiles of (*a*) $\bar{u}/U_0$ (*b*) $(\overline{u'^2})^{1/2}/U_0$, (*c*) $\bar{\omega}R_0/U_0$ *vs.* y/δ_1 at six stations along the Stratford ramp. ○, $x/R_0 = 0.07$; ●, 0.22; ◇, 0.38; ×, 0.54; +, 0.70; △, 0.86. Left: $\alpha = 0$; right: $\alpha = 3°$, leeward side.

with a mean value of 2.62. These values are characteristic of a strongly retarded attached flow. For the leeward side at angle of attack, figures 15(*a*) and 15(*b*) suggest the separation point to be near $x/R_0 \approx 0.25$. At this location, $H \approx 3.38$. In the range of $x/R_0 = 0.2$–1, the shape factor is in the range 2.94–3.93 and its average value is 3.41.

Another series of measurements is performed to determine the total drag on the body fitted with the three different ramps. For this set of measurements, the sting is eliminated and the body is suspended by four wires as shown in figure 19, which allows it to be deflected in the downstream direction under the effect of the drag forces.

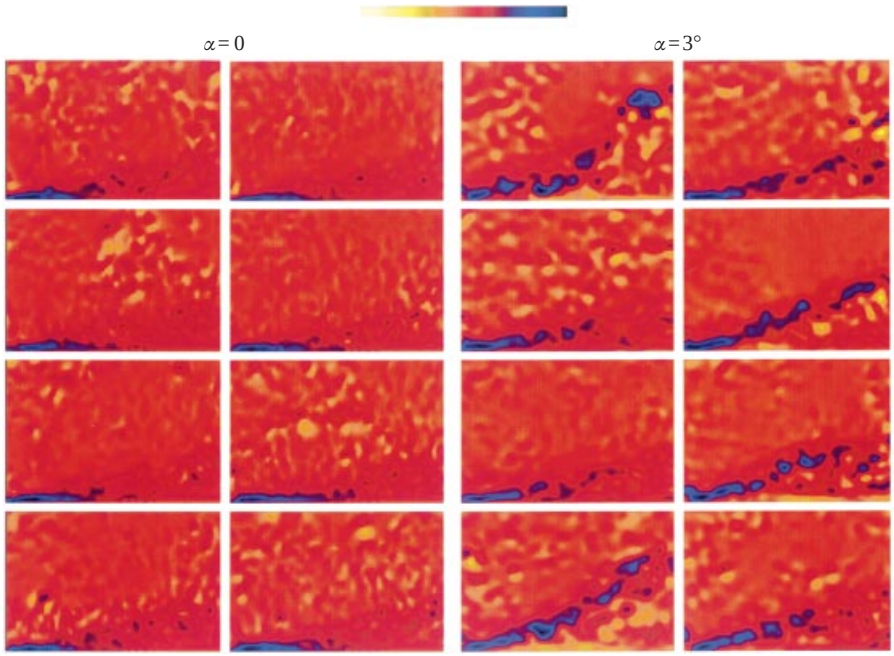

FIGURE 16. Comparison of eight instantaneous measurements of $\bar{\omega}$ over the Stratford ramp at $\alpha = 0$ and 3°.

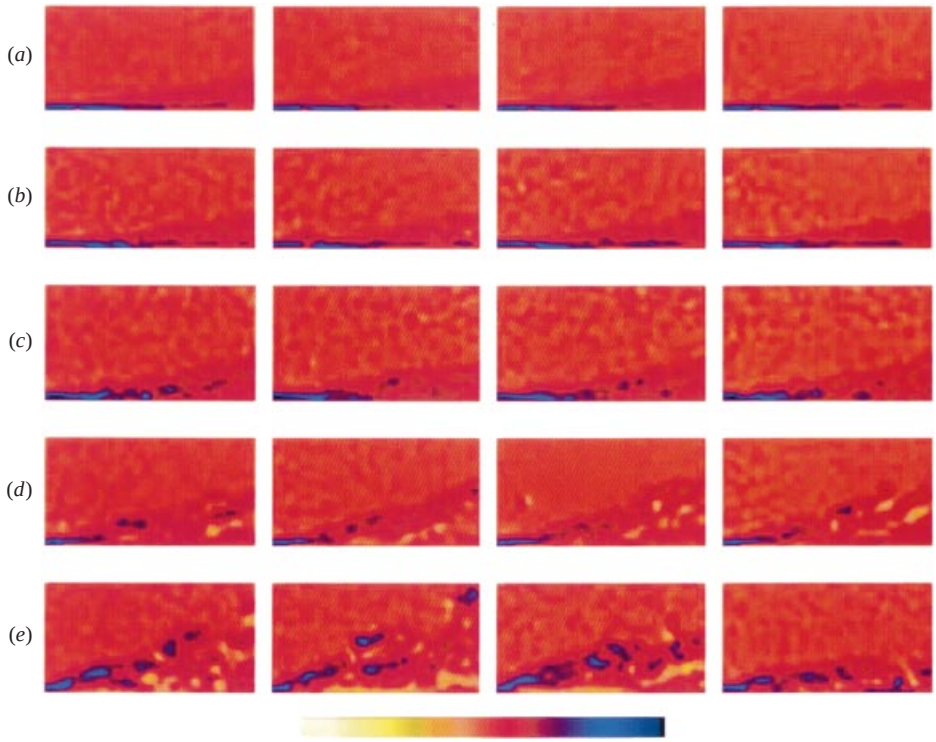

FIGURE 20. Four sample instantaneous maps of ω over the different ramps, sorted by increasing degree of ramp steepness: (*a*) conservative ramp, (*b*) windward side of Stratford ramp at $\alpha = 3°$, (*c*) Stratford ramp, $\alpha = 0$, (*d*) leeward side of Stratford ramp at $\alpha = 3°$, (*e*) radical ramp.

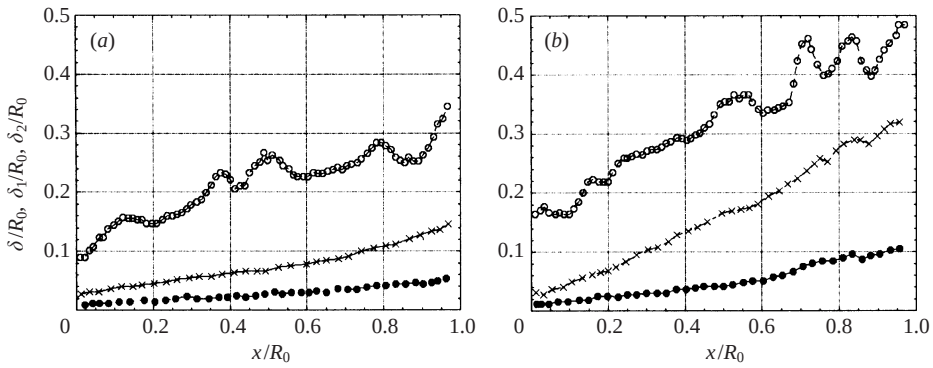

FIGURE 17. Downstream evolution of the time-averaged values of δ (●), δ_1 (×) and δ_2 (○) over the Stratford ramp at (*a*) $\alpha = 0$ and (*b*) $\alpha = 3°$.

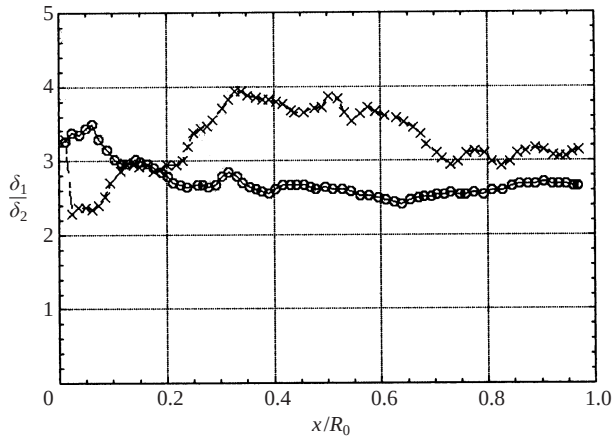

FIGURE 18. Shape factor of the boundary layer over the Stratford ramp. ○, $\alpha = 0$; ×, $\alpha = 3°$.

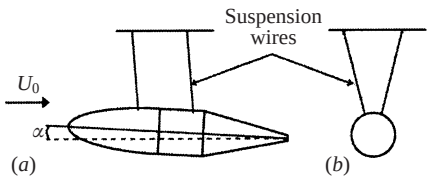

FIGURE 19. Body suspended by wires; (*a*) side view and (*b*) front view.

A calibration curve establishing the relationship between deflection and drag force is obtained by applying known forces to the body. To measure small displacements accurately, the body is imaged with a CCD camera equipped with a zoom lens before and after the flow is turned on. A comparison of the body position with and without airflow yields the displacement in pixels that is converted to physical units. Since the total drag includes the drag of the body and that of the suspension wires, the contribution of the wires, determined from circular-cylinder drag coefficient data, is subtracted. The suspension wires have a diameter of 0.81 mm, and an associated drag coefficient estimated at $C_D \simeq 1.0$ (from data on circular cylinders normal to the free stream).

Ramp	C_D
Stratford	0.083
Conservative	0.088
Radical	0.250

TABLE 2. Drag coefficients for the various ramps at $\alpha = 0$.

The values of the total drag coefficients based on frontal area are summarized in table 2. The Stratford ramp has the lowest drag, followed closely by the conservative ramp. This may be attributed to the fact that while the conservative ramp is not as efficient in reducing the mean wall shear stress as the Stratford ramp over its upstream portion, it does become Stratford-like over the downstream half. It could also be argued that the wake of the conservative ramp remains small, which helps it achieve a relatively low drag. The radical ramp clearly experiences a much higher drag due to flow separation. For comparison purposes, the drag coefficient of a smooth sphere at the same Reynolds number is approximately 0.3.

4. Discussion

4.1. *Stratford–Smith design criterion*

We have demonstrated flow over a variety of axisymmetric body closures designed to test the ideas put forth by Stratford (1959*a*, *b*) and by Smith (1977). The Stratford–Smith closure is intended to be the most rapid pressure recovery possible while just avoiding boundary layer separation. When applied to our specified forebody shape – a semi-ellipsoid plus cylinder – the predicted ramp shape is nearly conical with a cone half-angle of about 26.6°. The shape is the result of the design procedure discussed in great detail by Tokumaru *et al.* (1996). Figure 3(*b*) gives the body radius as well as its first and second derivatives expressed as functions of the axial coordinate X from the origin of the ramp. All dimensions are scaled by R_0.

If the initial fore-body shape is altered, the Stratford–Smith closure will be different, as several cases in Tokumaru *et al.* (1996) demonstrate. Generally speaking, however, there seems to be less curvature in the axisymmetric closures than in their two-dimensional counterparts (e.g. Liebeck 1973; Elsberry *et al.* 2000).

Four ramps have been described. Three are the Stratford–Smith ramp, the conservative or slightly lengthened version, and the radical, or slightly shortened version. The fourth ramp – also more radical that the Stratford–Smith design – is produced on the leeward side of the model by setting an angle of attack, $\alpha = 3°$. The flow-field velocity measurements we have described are able to show significant differences between these cases. The observations give a global measure of support to the original design proposition in the following way.

For the Stratford–Smith design, the boundary layer is able to 'turn the corner' at the origin of the ramp. The boundary layer displacement thickness is initially of the order of 1% of the body radius, and remains thin beyond the initial turn. In fact the boundary layer thickness, the displacement thickness and momentum thickness appear to decrease slightly just downstream from the turn, although our resolution in this region is lower than elsewhere.

On the Stratford–Smith ramp the inviscid flow external to the boundary layer turns smoothly. The pressure increase along the ramp is near the predicted value, and the

skin friction coefficient rapidly falls to and maintains a value estimated to be smaller than 10^{-4}.

On the radical ramp there is a much more rapid growth in boundary layer thickness beginning immediately at the origin of the ramp. The mean velocity field and the mean vorticity field both indicate the presence of separation, or at least the presence of a separation bubble. The estimated skin friction falls very close to zero in the region $x/R_0 = 0.4$–0.8. A 'separation bubble' description may be misleading however, for it evokes the notion of a somewhat benign local effect. In fact, a sequence of images of the instantaneous vorticity field suggest the presence of a transitory separation – that is, the flow is highly unsteady and completely separated at least part of the time.

At 3° angle of attack, the leeside flow on the Stratford–Smith ramp shows evidence of persistent separation and shear-layer-like behaviour in all the field measurements. In this sense, it is more radical than the shortened ramp. The eight instantaneous measurements of the vorticity field displayed on the right-hand side of figure 16 are particularly dramatic in illustrating the separation.

Thus a 15% shorter ramp or a ramp at angle of attack of perhaps 3° will contain regions of separated flow and will definitely not perform as well. In this sense, the Stratford–Smith ramp is near the limiting value, and is probably the shortest ramp that can be practically utilized.

The penalty for missing the design point on the conservative side is not nearly so great. The major distinction between the conservative ramp and the Stratford–Smith ramp is that the boundary layer grows more slowly over the slightly longer ramp, the ramp does not achieve the low skin friction value attained by the design ramp, and the body has a slightly larger overall drag coefficient.

4.2. *Comparisons with the two-dimensional Stratford ramp*

A recent paper by Elsberry *et al.* (2000) describes details of boundary layer flow in a strongly retarding pressure gradient, and it is worth pointing out similarities and differences between the present results and this excellent study. Other recent experimental studies of boundary layer flow in strongly retarding pressure gradients are Dengel & Fernholz (1990), and Skare & Krogstad (1994). In each, a condition near equilibrium (equilibrium in the Clauser sense) is established. Since the focus is somewhat different from our present intent of producing the most rapid pressure rise possible, these two experiments will not be discussed further. We recommend both papers to interested readers.

Elsberry *et al.* (2000, referred to as ELZW), utilize a two-dimensional ramp and a trial-and-error procedure to obtain the most severe pressure gradient possible while just avoiding separation. Measurements are made on the curved ramp, as were Stratford's original measurements.

Table 3 lists the pertinent information for the two experiments. For ELZW, two results are given: case A and case B, derived from an artificially thickened boundary layer. For our experiment, the case described is the Stratford–Smith ramp at $\alpha = 0$ (and with thin trip at $2.34R_0$ upstream from the ramp, as discussed in § 3.1). The second row in table 3 gives the total pressure rise across the recompression region, ΔC_p, in units of dynamic pressure at the inception of the pressure rise. Liebeck (1973) terms this quantity the roof-top q, and the corresponding velocity the roof-top velocity. Remembering that our reference velocity and dynamic pressure are values corresponding to the free stream, our results are re-scaled to reflect roof-top conditions just ahead of the ramp – $U_{local}/U_0 = 1.107$. ΔC_p is a measure of the efficiency of the ramp as a means for increasing static pressure.

Attribute	ELZW	Present
Geometry	Curved 2-D Stratford ramp	Axisymmetric Stratford–Smith ramp
Total pressure rise ΔC_p Referred to roof-top q_{total}	≈ 0.58 (case A) ≈ 0.48 (case B)	≈ 0.36
Minimum C_f in region of interest, τ_{wall}/q_{local}	3×10^{-4} (case A) 2×10^{-4} (case B)	6×10^{-5}
Pressure gradient, $\beta = (\delta_1 \, \mathrm{d}P/\mathrm{d}x)/\tau_{wall}$	≈ 36 (case A) ≈ 90 (case B)	≈ 250
Typical value of δ_1/body radius	—	0.1 (half-way along ramp)
Growth of displacement thickness, $\delta_{final}/\delta_{initial}$	≈ 9 (A and B linear growth)	≈ 9 (faster than linear growth)
Shape factor, δ_1/δ_2	2.4–2.4 (case A) 2.5–2.6 (case B)	2.6
Peak fluctuation, u_{rms}/U_{local}	0.10–0.11 (case A) 0.12–0.13 (case B)	$0.08 - 0.10$
Location of peak fluctuation, y/δ_1	1.0–1.2	1.0
Location of peak in $\mathrm{d}U/\mathrm{d}y$	—	1.0

TABLE 3. Comparison of two-dimensional and axisymmetric ramps.

Again, for comparison purposes, we have referenced skin friction and fluctuation values (rows 3 and 8) to the appropriate roof-top (local) condition. The fourth row is a global value of the commonly used pressure gradient parameter, β. It is defined here as the total pressure rise (row 2) over the length of the pressure rise region expressed in units of an average displacement thickness, and divided by the minimum attained value of the wall shear stress (row 3):

$$\beta = \frac{(\delta_1)_{average} \Delta P / \Delta X}{\tau_{wall}} = \frac{(\delta_1)_{average} \Delta C_p / \Delta X}{(C_f)_{min}}. \tag{4.1}$$

Small to moderate values of β measure the ability of the rapidly applied pressure gradient to modify the pre-existing structure of the boundary layer. In his excellent discussion of boundary layer fundamentals in Rosenhead (1963, chap. II) Lighthill has suggested that the pressure gradient can be equated to the presence of a source of vorticity at the wall. This would remain true for a turbulent boundary layer. Thus β becomes proportional to [wall vorticity source strength]/[wall vorticity].

The value of wall vorticity is determined by the magnitude of the wall source strength and by the ability of vorticity to diffuse toward (or away from) the wall. For sufficiently large values of β, the value of wall vorticity is dominated by the magnitude of the wall source strength.

Broadly speaking, there is similarity between the two experiments. Judging from the measured skin friction (row 3), ELZW case B and the present are closest to zero skin friction. Shape factors (row 7) bear out this conclusion. On the basis of the values of β, we would expect the largest departures from a conventional boundary layer shape to occur in ELZW case B and in the present experiment. ELZW note a significant extent of logarithmic behaviour in the velocity profiles near the wall for

case A. There is less of a logarithmic region present in ELZW case B, and there is no clearly displayed log region in our velocity profiles.

The magnitude of the peak longitudinal fluctuation (row 8) is lower in our observations than for the two-dimensional ramp. In addition, there is a curious difference between ELZW case A and case B. For the large values of β attained in ELZW case B and in the present experiment, it is perhaps not surprising that the flow would have insufficient time to establish a local equilibrium.

It is noted that the flow is extremely sensitive to small changes in surface shape (pressure gradient). This sensitivity is evident in our comparisons of the radical ramp, conservative ramp and Stratford ramp at angle of attack. We believe this lack of local similarity, and the sensitivity to small changes in surface shape, may be associated with the degree of flow unsteadiness that can take place within the boundary layer. The wall shear stress is so close to zero that even if the flow is not separated in a time-mean sense, the flow must reverse direction near the wall at such times, and these transitory reversals may be associated with locally elevated fluctuation levels. Elevated fluctuation levels in the outer portion of the boundary layer may thus reflect the severity of flow reversal events. As a final illustration, four sample plots of the instantaneous vorticity magnitude over each ramp are shown in figure 20. The data are sorted in terms of increasing ramp angle, and to the four cases previously discussed we have added data from the windward and leeward sides of the Stratford–Smith ramp at $\alpha = 3^\circ$. For the conservative ramp the vorticity is confined to a thin layer near the wall. As the ramp steepness increases, the vorticity gradually moves away from the wall, toward the outer edge of the boundary layer. In the case of the Stratford–Smith ramp at $\alpha = 0$ the vorticity seems to be organized in well-defined structures in the middle of the layer, which is believed to play an important role in keeping the boundary layer on the verge of separation. The radical ramp and the leeward side of the pitched ramp are both characterized by a loss of the organized nature of the vortical structures, as vorticity shifts dramatically away from the wall in a highly intermittent fashion.

The authors wish to acknowledge the financial support of the Office of Naval Research under Contract N00014-94-1-0590.

REFERENCES

Dengel, P. & Fernholz, H. H. 1990 An experimental investigation of an incompressible turbulent boundary layer in the vicinity of separation. *J. Fluid Mech.* **212**, 615–636.

Elsberry, K., Loessler, J., de Zhou, M. & Wygnanski, I. 2000 An experimental study of a boundary layer that is maintained on the verge of separation. *J. Fluid Mech.* **423**, 227–261 (referred to herein as ELZW).

Fincham, A. M. & Spedding, G. R. 1997 Low cost, high resolution DPIV for measurement of turbulent fluid flow. *Exps. Fluids* **23**, 449–462.

LeBlanc, P., Blackwelder, R. & Liebeck, R. 1990 A comparison between boundary layer measurements in a laminar separation bubble flow and linear stability theory calculations. In *Conference on Low Reynolds Number Aerodynamics* (ed. T. J. Mueller), pp. 337–353. Springer.

Liebeck, R. H. 1973 A class of airfoils designed for high lift in incompressible flow. *AIAA Paper* 73–86.

Patel, V. C., Nakayama, A. & Damian, R. 1974 Measurements in the thick axisymmetric turbulent boundary layer near the tail of a body of revolution. *J. Fluid Mech.* **63**, 345–367.

Rosenhead, L. (Ed.) 1963 *Laminar Boundary Layers.* Oxford University Press.

Schlichting, H. 1979 *Boundary Layer Theory*, 7th edn. McGraw-Hill.

Skare, P. E. & Krogstad, P.-A. 1994 A turbulent boundary layer near separation. *J. Fluid Mech.* **272**, 319–348.

Smith, A. M. O. 1977 Stratford's turbulent separation criterion for axially-symmetric flows. *Z. Angew. Math. Phys.* **28**, 929–939.

Spalart, P. R. & Leonard, A. 1987 Direct numerical simulation of equilibrium turbulent boundary layers. In Turbulent Shear Flows 5, pp. 234–252. Springer.

Stratford, B. S. 1959*a* The prediction of separation of the turbulent boundary layer. *J. Fluid Mech.* **5**, 1–16.

Stratford, B. S. 1959*b* An experimental flow with zero friction throughout its region of pressure rise. *J. Fluid Mech.* **5**, 17–35.

Tokumaru, P. T., Browand, F. K. & Blackwelder, R. F. 1996 The design of axisymmetrical body shapes having the Stratford–Smith pressure recovery. *AIAA Paper* 96-0551.

Zhang, H. L. & Fasel, H. F. 1997 Direct numerical simulation of two-dimensional incompressible laminar flow over Stratford ramp. In *Bull. Am. Phys. Soc./Div. Fluid Dyn.*, Vol. 42, No. 11.